

EAVN Astrometry toward the Extreme Outer Galaxy: Kinematic distance with the proper motion of G034.84–00.95

Nobuyuki SAKAI^{1, 2}, Bo Zhang³, Shuangjing Xu^{1, 3}, Daisuke SAKAI^{4, 5}, Yoshiaki TAMURA⁴, Takaaki JIKE⁴, Taehyun Jung¹, Chungsik Oh¹, Jeong-Sook Kim⁶, Noriyuki KAWAGUCHI⁷, Hiroshi IMAI⁸, Wu JIANG³, Lang CUI⁹, Soon-Wook Kim¹, Pengfei JIANG⁹, Tomoharu Kurayama¹⁰, Jeong Ae Lee¹, Kazuya Hachisuka⁴, Dong-Kyu Jung¹, Bo Xia³, Guanghui Li⁹, Mareki Honma⁴, Kee-Tae Kim¹, Zhi-Qiang Shen^{3, 11}, and Na Wang^{9, 11}.

¹Korea Astronomy & Space Science Institute, 776, Daedeokdae-ro, Yuseong-gu, Daejeon 34055, Korea

²National Astronomical Research Institute of Thailand (Public Organization), 260 Moo 4, T. Donkaew, A. Maerim, Chiang Mai, 50180, Thailand

³Shanghai Astronomical Observatory, Chinese Academy of Sciences, 80 Nandan Road, Shanghai, 200030, China

⁴Mizusawa VLBI Observatory, National Astronomical Observatory of Japan, 2-12 Hoshigaoka, Mizusawa, Oshu, Iwate 023-0861, Japan

⁵The Iwate Nippo Co., Ltd., 3-7 Uchimaru, Morioka, Iwate 020-8622, Japan

⁶Ulsan National Institute of Science and Technology UNIST-gil 50, Eonyang-eup, Ulju-gun, Ulsan 44919, Republic of Korea

⁷Mizusawa VLBI Observatory, National Astronomical Observatory of Japan, 2-21-1 Osawa, Mitaka, Tokyo 181-8588, Japan

⁸Amanogawa Galaxy Astronomy Research Center, Graduate School of Science and Engineering, Kagoshima University, 1-21-35 Korimoto Kagoshima

⁹Xinjiang Astronomical Observatory, Chinese Academy of Sciences, Urumqi 830011, China

¹⁰Faculty of Education and Human Sciences, Department of School Education, Teikyo University of Science, 2-2-1 Senju-Sakuragi, Adachi, Tokyo 120-0045, Japan

¹¹Key Laboratory of Radio Astronomy, Chinese Academy of Sciences, Nanjing 210008, China

*E-mail: nobuyuki@narit.or.th

Received 19 August 2022; Accepted 21 November 2022

Abstract

We aim to reveal the structure and kinematics of the Outer-Scutum-Centaurus (OSC) arm located on the far side of the Milky Way through very long baseline interferometry (VLBI) astrometry using KaVA, which is composed of KVN (Korean VLBI Network) and VERA (VLBI Exploration of Radio Astrometry). We report the proper motion of a 22 GHz H₂O maser source, which is associated with the star-forming region G034.84–00.95, to be $(\mu_{\alpha} \cos \delta, \mu_{\delta}) = (-1.61 \pm 0.18, -4.29 \pm 0.16)$ mas yr⁻¹ in equatorial coordinates (J2000). We estimate the 2D kinematic distance to the source to be 18.6 ± 1.0 kpc, which is derived from the variance-weighted average of kinematic distances with LSR velocity and the Galactic-longitude component of the measured proper motion. Our result places the source in the OSC arm and

implies that G034.84–00.95 is moving away from the Galactic plane with a vertical velocity of $-38 \pm 16 \text{ km s}^{-1}$. Since the H I supershell GS033+06–49 is located at a kinematic distance roughly equal to that of G034.84–00.95, it is expected that gas circulation occurs between the outer Galactic disk around G034.84–00.95 with a Galactocentric distance of $12.8_{-0.9}^{+1.0}$ kpc and halo. We evaluate possible origins of the fast vertical motion of G034.84–00.95, which are (1) supernova explosions and (2) cloud collisions with the Galactic disk. However, neither of the possibilities are matched with the results of VLBI astrometry as well as spatial distributions of H II regions and H I gas.

Key words: Galaxy: disk—Galaxy: kinematics and dynamics—proper motions—masers—instrumentation: interferometers

1 Introduction

Gaia satellite and VLBI arrays have measured trigonometric parallaxes with accuracies of 10 microarcsecond (μas) or better for stars and masers associated with star-forming regions, respectively (e.g. Gaia Collaboration 2022; Reid et al. 2019; VERA Collaboration et al. 2020). This allows us to make a 3D map of the Milky Way. However, the current parallax measurements are conducted mostly within 10 kpc from the Sun, which delineates roughly one-third of the Galactic disk (e.g., see Fig. 1 of Reid et al. 2019). Yamauchi et al. (2016) measured the proper motion of G007.47+00.06 with VERA (VLBI Exploration of Radio Astrometry), and estimated a source distance of 20 ± 2 kpc based on the LSR velocity and proper motion in the direction of Galactic longitude (i.e., 2D kinematic distance). Sanna et al. (2017) confirmed the validity of the 2D kinematic distance via a trigonometric parallax distance measurement of the same source, which was derived to be $20.4_{-2.2}^{+2.8}$ kpc with VLBA (Very Long Baseline Array). The reliability of 2D/3D kinematic distance was evaluated and confirmed for sources well past the Galactic center by Reid (2022). Their work showed that 3D kinematic distances are more accurate than can be achieved with parallax measurements for distant sources. There is only one astrometric result (i.e., G007.47+00.06) in the outer portion of the Scutum-Centaurus arm while there are ~ 40 astrometric results in the inner portion of the Scutum-Centaurus arm. To better understand the nature of the outer portion of the Scutum-Centaurus arm, it is necessary to increase the number of astrometric results for the outer portion of the arm.

The Extreme Outer Galaxy (EOG) is defined as the region outside the Outer spiral arm or at a Galactocentric distance $R \geq 2R_0$ where R_0 is the Galactocentric distance to the Sun (Digel et al. 1994). Dame & Thaddeus (2011) found a new molecular arm beyond the Outer arm in the first Galactic quadrant and the arm is currently called the Outer-Scutum-Centaurus (OSC) arm. Also, Sun et al. (2015, 2017) discovered 72 EOG clouds (CO J = 1-0) in the second Galactic quadrant and 168 EOG clouds (^{12}CO and ^{13}CO J = 1-0) in the Galactic longitude range $34.75^\circ \leq l \leq 45.25^\circ$. All the CO clouds detected

by Sun et al. (2015, 2017) are associated with the OSC arm on the basis of a position-velocity diagram of CO (i.e., Galactic longitude l vs. LSR velocity v). Excited-state OH (4.8 GHz), CH_3OH (6.7 GHz) and H_2O (22 GHz) masers were discovered toward brighter and massive EOG clouds by Sun et al. (2018), although there was a limited number of detections (i.e., seven).

Here note that some of the EOG sources are close to the celestial equator $|\delta_{J2000}| < 9^\circ$, where making VLBI imaging is difficult. Kurayama et al. (2011) conducted VLBI astrometry toward a low-declination source, the star-forming region G034.43+00.24 ($\delta_{J2000} \sim 1^\circ$) with VERA. Their imaging analysis suffered from side lobes of the synthesized interferometry beam pattern along the declination direction (see Fig. 7 of Kurayama et al. 2011), and they could use only astrometric results in the direction of right ascension for measuring the parallax of the source. To suppress the effect of such side lobes, increase in the number of antennas and an array configuration with minimum baseline redundancy are important. This is attributed to the fact that the width in v direction is equal to that in the u direction times the sine of the declination δ in the (u, v) coverage (Thompson et al. 2017). If we observe a source with a declination of 0 degree using the four telescopes of VERA, we can obtain only six v values. On the other hand, we can obtain 21 v values when observing the same source with KaVA (KVN and VERA Array), where KVN is the Korean VLBI Network.

In this paper, we report new astrometric results for H_2O masers associated with the star-forming region G034.84-00.95. G034.84–00.95 is associated with the OSC arm on the l - v plot of CO, and the source emits H_2O (22.2 GHz) and OH (4.8 GHz) masers (Sun et al. 2018). The detection of OH masers suggests that the source is a more evolved star-forming region (Ouyang et al. 2022). Robitaille et al. (2008) classified the source as Young Stellar Object based on its infrared color $[8.0] - [24.0] \geq 2.5$ and magnitude $[4.5] > 7.8$. However, no detailed research has been conducted for the source, besides survey results.

We describe our observational setup and data reduction in sections 2 and 3, respectively. The astrometric results are shown in section 4. We discuss the validity of our astrometric results as

Table 1. Observational information.

Source	R.A. (J2000) hh:mm:ss	Decl. (J2000) dd:mm:ss	Obs. Date in UT 20yy/mm/dd	Participating antenna	Flux density (Jy/beam)	S/N	
						G034	J1851
G034.84–00.95	18:58:17.673	+01:16:06.40	A. 19/09/05	123-- 67--	1.6	7	75
			B. 19/10/11	12- 45 67--	1.5	12	108
			C. 19/11/04	12- 45 67--	2.0	20	213
			D. 19/12/21	12 3 45 67--	1.9	23	208
			E. 20/01/29	12 3 45 67--	2.2	34	271
			F. 20/02/27	12 3 45 67--	1.9	34	264
			G. 20/03/22	12 3 45 67--	2.0	29	289
			H. 20/04/19	12 3 45 6 [†] 7--	1.5	10	132
			I. 20/05/26	1-3 45 67--	–	< 5	164
			J. 20/09/22	1-3 45 6- 89	0.6	5	28
			K. 20/10/04	-23 4---89	–	< 5	113
			L. 20/11/12	1 23 4 5 6 7 89	2.4	21	200
			M. 20/12/07	-23 4 5 6 7--	–	Obs. failure	
			N. 21/01/27	1 23 4 5 [‡] 6 [‡] 7 [‡] 8 [‡] –	–	< 5	96
			O. 21/03/23	1 23 4 5 [‡] 6 [‡] 7 [‡] 8 [‡] 9 [‡]	2.2	6	74

Column 1 : 22 GHz H₂O maser source; Columns 2-3: equatorial coordinates in (J2000); Column 4: observation date in UT; Column 5: participating antennas (1 = Mizusawa; 2 = Iriki; 3 = Ogasawara; 4 = Ishigaki; 5 = Yonsei; 6 = Ulsan; 7 = Tamna; 8 = Tianma; 9 = Nanshan); Column 6: flux density of the maser source; Columns 7-8: Signal to noise ratio values of the maser and a phase reference (i.e., J1851+0035) image where the maser is phase referenced to the continuum source.

[†] Fringe of a bright calibrator was not detected in KVN Ulsan data.

[‡] Only VERA data could be used because fast antenna switching was not employed in the other stations. VERA joined the observations using the dual-beam system, and those observations were conducted for surveying new targets (see the text for details).

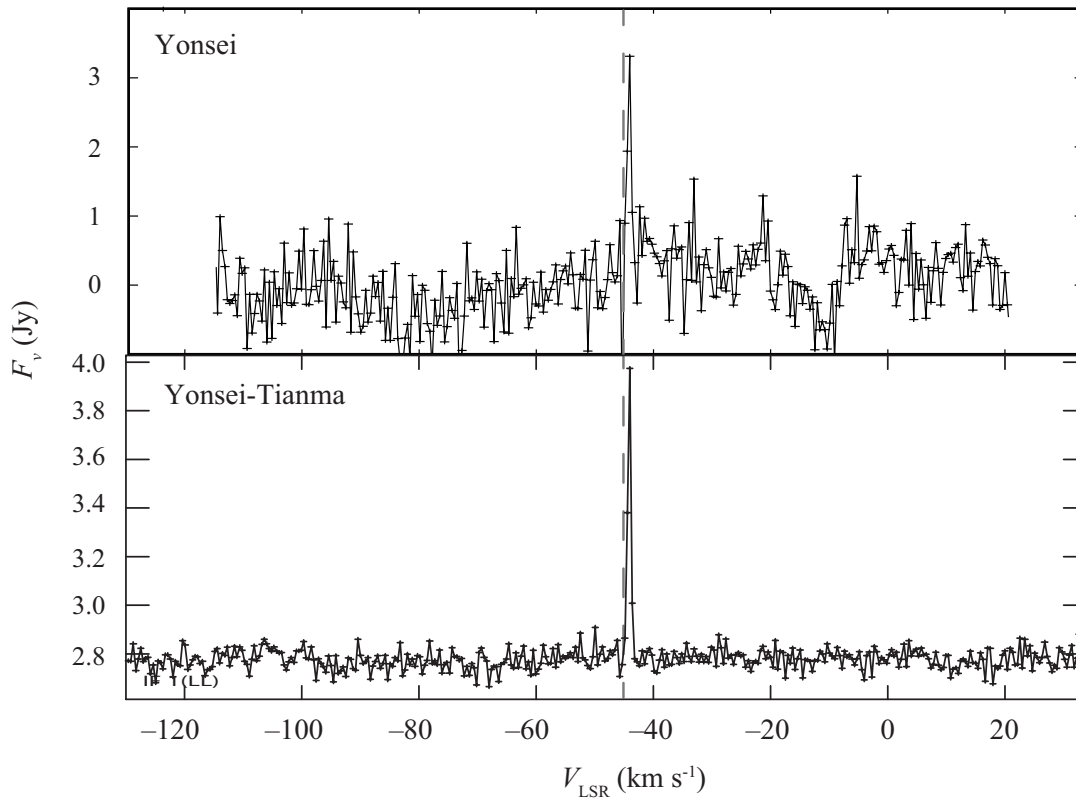


Fig. 1. Total and cross-power spectra of G034.84–00.95 are shown with Yonsei (Top) and Yonsei-Tianma baseline (Bottom), respectively. In the total power spectrum, data around both edges are not shown due to imperfect baseline subtraction. The observational data of epoch L is used (see Table 1). Vertical dashed lines indicate the systemic velocity of G034.84–00.95 which was determined by ¹²CO(J=1–0) observations (-45.1 ± 2.2 km s⁻¹; Sun et al. 2017).

well as the structure and kinematics of the OSC arm in section 5. In section 6, we summarize the paper.

2 Observations

Fifteen astrometric observations of 22 GHz H₂O masers associated with G034.84–00.95 were carried out between the 5th of September 2019 and the 23rd of March 2021 using KaVA which is part of the EAVN (East Asian VLBI Network)¹. CVN (Chinese VLBI Network) telescopes Tianma 65m and Nanshan 26m have joined the KaVA astrometric observations since the 25th of May 2020. Observational information is shown in Table 1. We observed the maser source as well as phase references J1851+0035 (α, δ)_{J2000.0} = (18^h51^m46^s.7231, +00°35′32″.364) and J1851+0035 (α, δ)_{J2000.0} = (18^h58^m02^s.3528, +03°13′16″.301) for relative VLBI astrometry². Separation angles between the target and the phase references are 1.8° and 2.0°, respectively. Note that J1858+0313 was observed in only eight epochs (i.e., epochs A–C and I–M in Table 1). While VERA used the dual beam system (Kawaguchi et al. 2000) to simultaneously observe the target and a phase reference source, KVN employed fast antenna switching with a cycle of 1 (min) (20 seconds on target; 10 seconds antenna slewing; 20 seconds on a phase reference and a further 10 seconds antenna slewing). After the observational epoch “I” in Table 1, KVN and CVN employed the fast antenna switching with a cycle of 80 (sec), except for observation epochs N and O in Table 1. We observed G034.84–00.95 as well as other sources (G039.18–01.43; G040.29+01.15; G040.96+02.48) in epochs N and O. Also, four half-hour “geodetic blocks” spaced by about 2 hr were inserted in epochs between J and M for clock and atmospheric (tropospheric) delay calibration of the EAVN. For calibration of electric phase differences (i.e., manual phase calibration), a bright continuum source was observed for 5 (min) every ~80 (min) in all observations.

Left-handed circular polarization data were recorded at 1024 Mbps with 2-bit quantization and the data were correlated with KJCC hardware correlator (Lee et al. 2015). Details of the back-end systems for KaVA and CVN are summarized in the status report of the EAVN³. The maser data consisted of 16 MHz/1 IF and correlated with 512 channels, giving a frequency (velocity) spacing of 31.25 kHz (0.42 km s⁻¹) at a rest frequency of 22.235080 GHz (for H₂O maser). On the other hand, the continuum source data consisted of fifteen 16 MHz bands spanning 464 MHz where the fifteen IFs were distributed with an

evenly spaced gap of 16 MHz, and each IF was correlated with 64 channels.

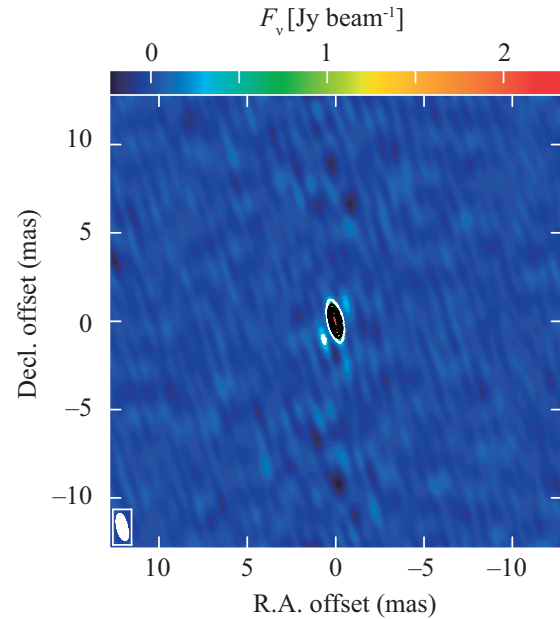


Fig. 2. EAVN self-calibration image of G034.84–00.95 for observational epoch ‘L’ (see Table 1). Contour levels start at the 10 σ level and increase by factors of 10. The pattern of source’s sidelobes, which is elongated from north-west to south-east directions, is due to the synthesized beam pattern.

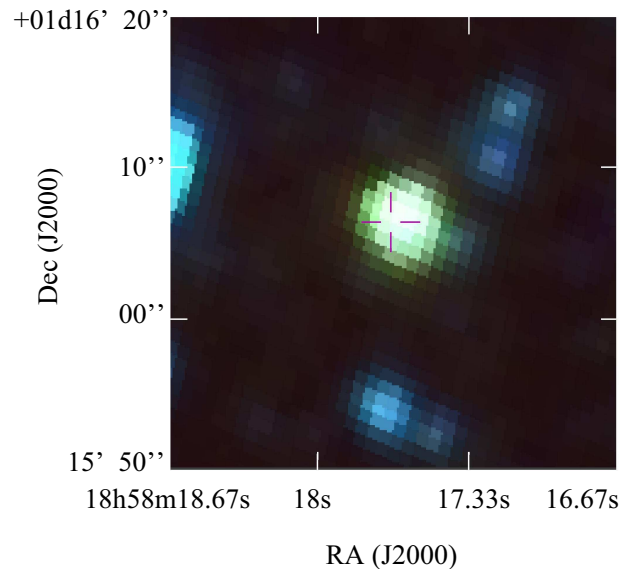


Fig. 3. *Spitzer* RGB mid-infrared image (8.0, 4.5 and 3.6 μ m) for the star-forming region G034.84–00.95 (Benjamin et al. 2003). The position of the 22 GHz water maser associated with G034.84–00.95, is emphasized by the cross symbol.

¹ see EAVN HP: https://radio.kasi.re.kr/eavn/main_eavn.php

² The positions of background continuum sources were obtained from the Radio Fundamental Catalog of Astrogeo Center: <http://astrogeo.org/rfc/>

³ https://radio.kasi.re.kr/status_report/files/status_report_EAVN_2022B.pdf

3 Data reduction

Using the NRAO Astronomical Image Processing System (AIPS; van Moorsel et al. 1996), data reduction was conducted with a standard procedure (e.g., see Fig. 11 of Kurayama et al. 2011). Since *a-priori* delay model used in the correlation processing was not accurate enough for high precision astrometry, the correlator model was replaced with a precise delay model consisting of an up-to-date geodynamical model (McCarthy 1996), the Earth orientation parameter EOP 08 C04 (IAU1980; C. Bizouard & D. Gambis 2011⁴), station coordinates for KaVA antennas determined by Geodetic VLBI observations at K-band (the project's internal code v2005trf14; Jike et al. 2018), ionospheric delays (GIM produced by CODE, the Center for Orbit Determination in Europe)⁵, and zenith wet excess path delays measured with GPS and the JMA (Japan Meteorological Agency meso-scale analysis data for numerical weather prediction⁶). We applied GPS for VERA because the time resolution of GPS (5 min) was shorter than that of JMA (3 hr). On the other hand, we applied JMA-based corrections to KVN data since GPS data were unavailable during the observational period. Note that Nagayama et al. (2015) demonstrated that tropospheric zenith delay residual ($c\Delta\tau_{\text{trop}}$) can be suppressed within ~ 2 cm using either GPS or JMA.

The effect of the time variation of the parallactic angles of the telescope was corrected with the AIPS task CLCOR with the adverbs OPCODE = 'PANG' and CLCORPRM(1)=1, except for VERA where this effect does not appear thanks to the field rotator equipped for the VERA dual-beam system. As explained previously, KVN and CVN observed the maser source and a phase reference in fast antenna switching, whereas VERA observed both the sources simultaneously using the dual-beam system. Thus, we made a flag file (FG table) with the AIPS task UVFLG, which was applied for the antenna slew time of the KVN and CVN stations.

After standard instrumental delay calibration, phase-referencing procedures, and source image synthesis, the position of the maser source relative to a phase reference source was determined by an elliptical Gaussian fitting with the AIPS task "JMFIT" in each observation epoch. Regarding the phase-referencing procedure, we used solution derived for a nearby continuum source to phase reference the maser source. To guarantee the reliability of the data reduction (i.e., phase referenc- ing), we show corrected phases in Fig. 12 of Appendix 1.

Maser positions were recorded as a function of time and modeled by (1) an annual parallax, (2) linear proper motion components in east–west ($\alpha\cos\delta$) and north–south (δ) directions, and (3) reference positions in $\alpha\cos\delta$ (α_0) and δ (δ_0) (e.g.,

see equations 1-2 in Kamezaki et al. 2012). The model parameters were determined with a Bayesian approach (see Appendix 2 for details) where a systematic error was added in quadrature to a formal (thermal) error so that the reduced chi-square value became nearly unity. This is because systematic error caused by the tropospheric zenith delay residual is dominant in 22 GHz VLBI astrometry for distant sources (e.g., Nagayama et al. 2020).

4 Results

4.1 EAVN self-calibration results

Figure 1 shows total and cross-power spectra of the 22 GHz water maser in G034.84–00.95. We confirm the single peak emission whose velocity is consistent with the peak velocity of ^{12}CO (J=1–0) (-45.1 ± 2.2 km s⁻¹; Sun et al. 2017). Figure 2 displays an EAVN self-calibration image of G034.84–00.95 for the observational epoch 'L' (see the corresponding date in Table 1). We could make an image only for the peak emission. We confirmed that the signal to noise (S/N) ratio of the EAVN image was 1.3 times increased (46→60) compared to that of the KaVA image even though Tianma 65m and Nanshan 25m telescopes participated for only ~ 3 hours (roughly one third of the total observing time) in observational epoch L. We also confirmed that the maser spot was not resolved with the longest baseline length of 5200 km in Fig. 2. The maser spot is compact and suitable for parallax and proper-motion fitting.

4.2 KaVA astrometry results

We report only KaVA astrometric results in this paper since zenith wet delay calibration of EAVN (i.e., KaVA, Tianma 65m, and Nanshan 26m) based on the Geodetic blocks remains under evaluation. We successfully produced maser images with phase referenc- ing in 11 out of 15 observations (see Table 1). The position of the maser source is superimposed on a *Spitzer* RGB mid-infrared image (Fig. 3) where the angular resolution of the *Spitzer* image is 3 (arcsec) and the position of the maser source is consistent with that of the Spitzer/GLIMPSE source G034.8427-00.9465 within 0.4 (arcsec) (Spitzer Science 2009). Failures of the rest of the observations are due to insufficient signal to noise ratio (S/N < 5) of the phase-referenced (i.e., maser) image and incorrect frequency setup. We found correlation between S/N ratio values of images of the maser and a phase reference J1851+0035 with a correlation coefficient of 0.96 (see Table 1).

Figure 4 demonstrates that the side lobe along the north-south direction can be well suppressed in the KaVA dirty image. We confirmed that correlated flux density of the maser source was ~ 2 Jy beam⁻¹ at a line-of-sight velocity of $V_{\text{H}_2\text{O}}$

⁴ C. Bizouard & D. Gambis 2011: https://hpiers.obspm.fr/iiers/eop/eopc04_08/C04_guide.pdf

⁵ <http://aiuws.unibe.ch/ionosphere/>

⁶ <https://www.jma.go.jp/jma/jma-eng/jma-center/nwp/outline2019-nwp/index.htm>

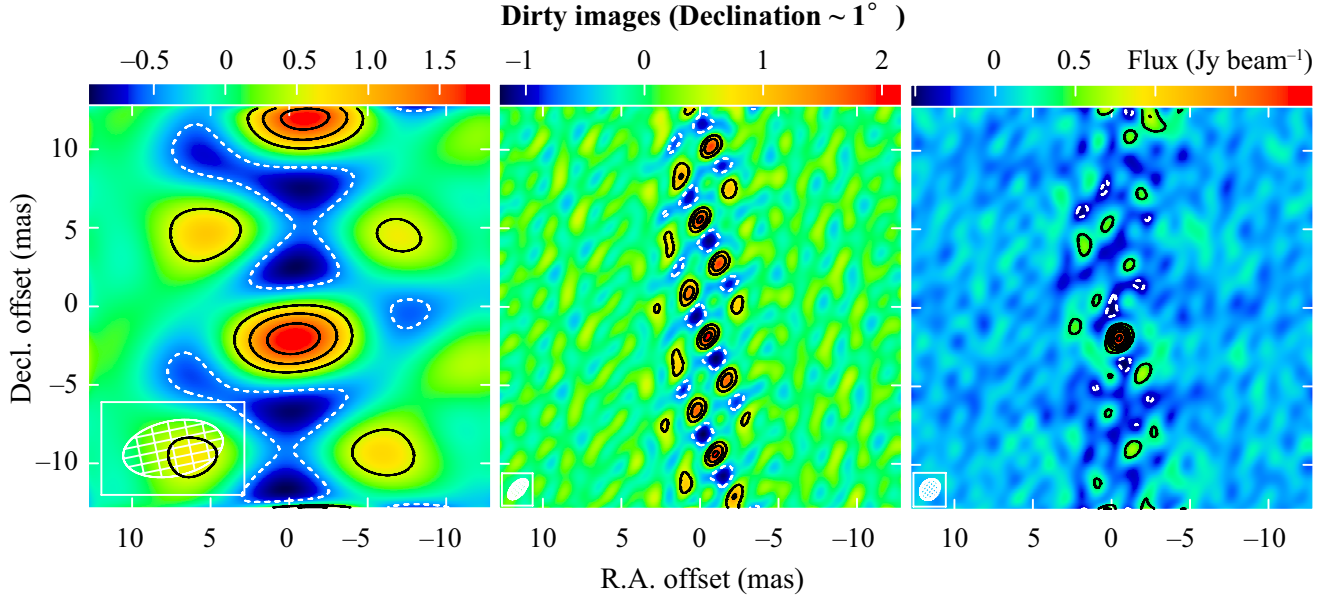


Fig. 4. Dirty images of G034.84–00.95 obtained with KVN (Left), VERA (Middle), and KaVA (Right), respectively. The observation was conducted on the 22nd of March 2020 (observation epoch G in Table 1). Solid lines show contour levels of the images with a step of 3σ noise level. The dashed lines are the same as the solid ones, but with a step of -3σ .

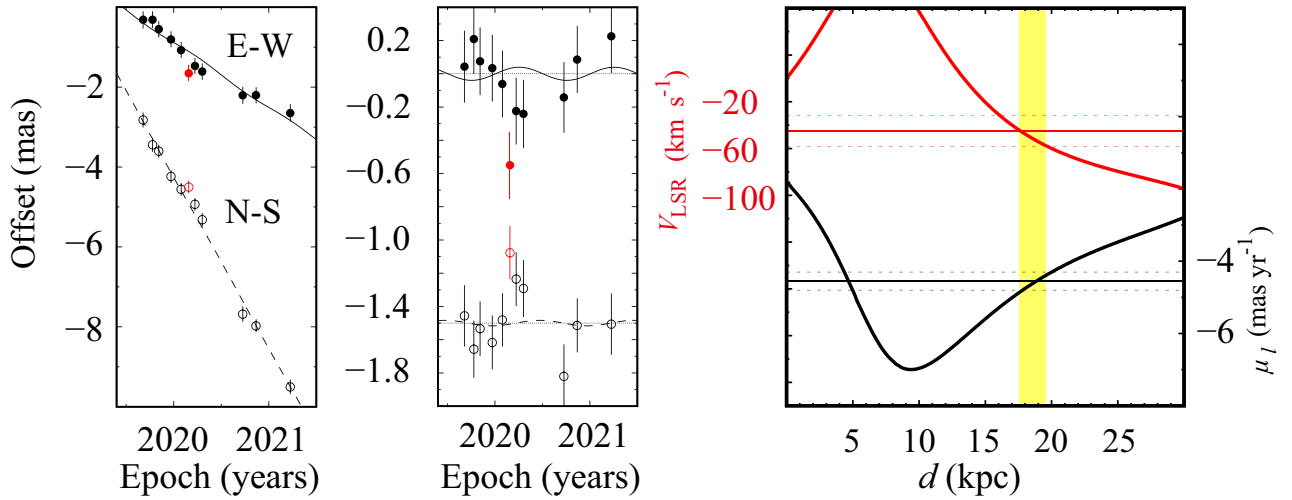


Fig. 5. (Left) Results of parallax and proper motion fittings for G034.84-00.95. The position offsets of the masers are plotted with respect to the background QSO J1851+0035 in the east ($\alpha\cos\delta$) and north (δ) directions as a function of time. For clarity, the northerly data is plotted with an offset from the easterly data. The best-fit models in the easterly and northerly directions are shown as continuous and dashed curves, respectively. The data points denoted by red circles are removed from the fitting using the “conservative formulation” of Sivia & Skilling 2006 (see Appendix 2 for details). (Middle) Same as the left, but with the fitted proper motion removed. (Right) Kinematic distance models through LSR velocity V_{LSR} (red curve; Y1 axis) and the proper motion in the direction of Galactic longitude μ_l (black curve; Y2 axis). The horizontal axis is the heliocentric distance. Here, we assume the Galactic constants to be ($R_0 = 8.15$ kpc, $\Theta_0 = 236$ km s $^{-1}$) and a universal rotation curve (A5 model of Reid et al. 2019). Horizontal red and black lines present the observed best values of V_{LSR} and μ_l , respectively. Dotted red lines represent the error range where ± 13 km s $^{-1}$ is added in quadrature to a formal error of V_{LSR} , while dotted black lines are the same as the red ones but for μ_l (see the text for details). The yellow shaded region indicates the range for the weighted average of the two kinematic distances.

Table 2. Parallax, proper motion, and kinematic distance results for G034.84–00.95.

Target	Parallax (π) [*] (mas)	$\mu_\alpha \cos \delta$ (mas yr ⁻¹)	μ_δ (mas yr ⁻¹)	V_{LSR} (km s ⁻¹)	Kinematic distance			Ref.
					$d_{V_{\text{LSR}}}$ (kpc)	d_{μ_l} (kpc)	d_{2D} (kpc)	
G034.84–00.95	0.040 ^{+0.061} _{-0.028}	-1.61±0.18	-4.29±0.16	-45.1±2.2	17.7 ^{+2.0} _{-1.6}	18.9±1.1	18.6±1.0	a

Column 1: 22 GHz H₂O maser source; Columns 2: parallax; Columns 3-4; proper motion components in east and north directions, respectively; Column 5: LSR velocity; Columns 6-7: kinematic distances through LSR velocity and proper motion in the direction of Galactic longitude, respectively (see the text for details); Column 8: the weighted average of both Columns 6 and 7; Column 9: reference for the LSR velocity estimated from a molecular line observation.

Reference: (a) Sun et al. (2017).

* Since the fractional parallax error is significantly greater than 20%, distance estimation by simply inverting the parallax results in a significant bias (see Bailer-Jones 2015).

~ -44 km s⁻¹ during the observations. The velocity of G034.84–00.95 is consistent with the LSR velocity of the source obtained by ¹²CO(J=1–0) observations (-45.1 ± 2.2 km s⁻¹; Sun et al. 2017).

We measured the proper motion components of the maser spot to be $(\mu_\alpha \cos \delta, \mu_\delta) = (-1.61 \pm 0.18, -4.29 \pm 0.16)$ mas yr⁻¹ in equatorial coordinates, however we could not obtain a reliable result of the parallax fitting (Table 2 and Fig. 5). Since H₂O masers are typically generated in outflows of tens of km s⁻¹ and transferring the motion of the maser to that of the central star causes an uncertainty, we adopted a measurement uncertainty of ± 10 km s⁻¹ in quadrature to each motion component in Table 2 by considering the fact that we detected only one maser spot throughout the observations. The systematic error of 10 km s⁻¹ is converted to 0.11 mas yr⁻¹ at a source distance of 18.9 kpc which is determined by the measured proper motion as explained below.

We estimated kinematic distances of the source through LSR velocity V_{LSR} and the proper motion in the direction of Galactic longitude μ_l by referring to Sakai et al. (2022) (see also Table 2). For estimating the kinematic distances, we assumed the solar motion to be $(U_\odot, V_\odot, W_\odot) = (10.6, 10.7, 7.6)$ km s⁻¹, the Galactic constants to be $(R_0, \Theta_0) = (8.15 \text{ kpc}, 236 \text{ km s}^{-1})$, and a universal rotation curve (i.e., A5 model of Reid et al. 2019). To allow the effect of noncircular motion caused by the spiral arm, we added 13 km s⁻¹ in quadrature to the formal error of V_{LSR} . The uncertainty of 13 km s⁻¹ corresponds to the mean noncircular motion of the outer Perseus arm (Sakai et al. 2019). The error range of μ_l was estimated in the same procedure. The resultant kinematic distances, $d_{V_{\text{LSR}}}$ and d_{μ_l} , are 17.7^{+2.0}_{-1.6} kpc and 18.9±1.1 kpc, respectively. The kinematic distance d_{μ_l} is more accurate than $d_{V_{\text{LSR}}}$ in the case of G034.84–00.95, since the accuracy distributions of d_{μ_l} and $d_{V_{\text{LSR}}}$ are different on the Galactic coordinates (see Sofue 2011). The two dimensional kinematic distance, d_{2D} , as the variance weighted average of both $d_{V_{\text{LSR}}}$ and d_{μ_l} , is 18.6±1.0 kpc. We further examined

the validity of our distance estimation in Appendix 3 where 2D kinematic distances are determined by shifting LSR velocity and the measured proper motion individually by 40 km s⁻¹. We confirmed that all the 2D kinematic distances are consistent within errors. Note that the validity of our distance estimate should be checked by measuring the trigonometric parallax of G034.84–00.95 in the future. The 2D kinematic distance (i.e., $d_{2D} = 18.6 \pm 1.0$ kpc) places the source in the Outer-Scutum-Centaurus arm (Fig. 6).

Note that the naming of “2D distance” comes from the fact that we didn’t consider the proper motion perpendicular to the disk (i.e., μ_b) in the distance estimation of G034.84–00.95, because the vertical motion is a weak constraint compared to other motion components V_{LSR} and μ_l in our case. To verify the above explanation, we used “A Parallax-based Distance Calculator⁷” (Reid et al. 2016, 2019) where “3D motion” is considered to estimate the distance of a source. We confirmed that the distance constraint by the vertical motion μ_b has a large tail in the probability density function of the distance. The resultant distance of the calculator is 18.5±1.0 kpc with a probability of 0.89, which is consistent with our independent estimate (18.6±1.0 kpc) within errors.

5 Discussion

5.1 Is G034.84-00.95 really a distant object ?

Although most CO clouds associated with the Outer-Scutum-Centaurus arm show positive Galactic latitude values at the Galactic longitude range $30^\circ \leq l \leq 42^\circ$, G034.84–00.95 has a negative Galactic latitude (see Fig. 7). This indicates that the source may be a nearby object, which is inconsistent with our distance estimate of the source ($d = 18.6 \pm 1.0$ kpc). Indeed, nearby star-forming regions G034.79–01.38 ($d = 2.62^{+0.15}_{-0.13}$ kpc; Reid et al. 2019) and G035.19–00.74 ($d = 2.19^{+0.24}_{-0.20}$ kpc; Reid et al. 2019) as well as the supernova remnant W44 ($d \sim 3.1$

⁷ <http://bessel.vlbi-astrometry.org/node/378>

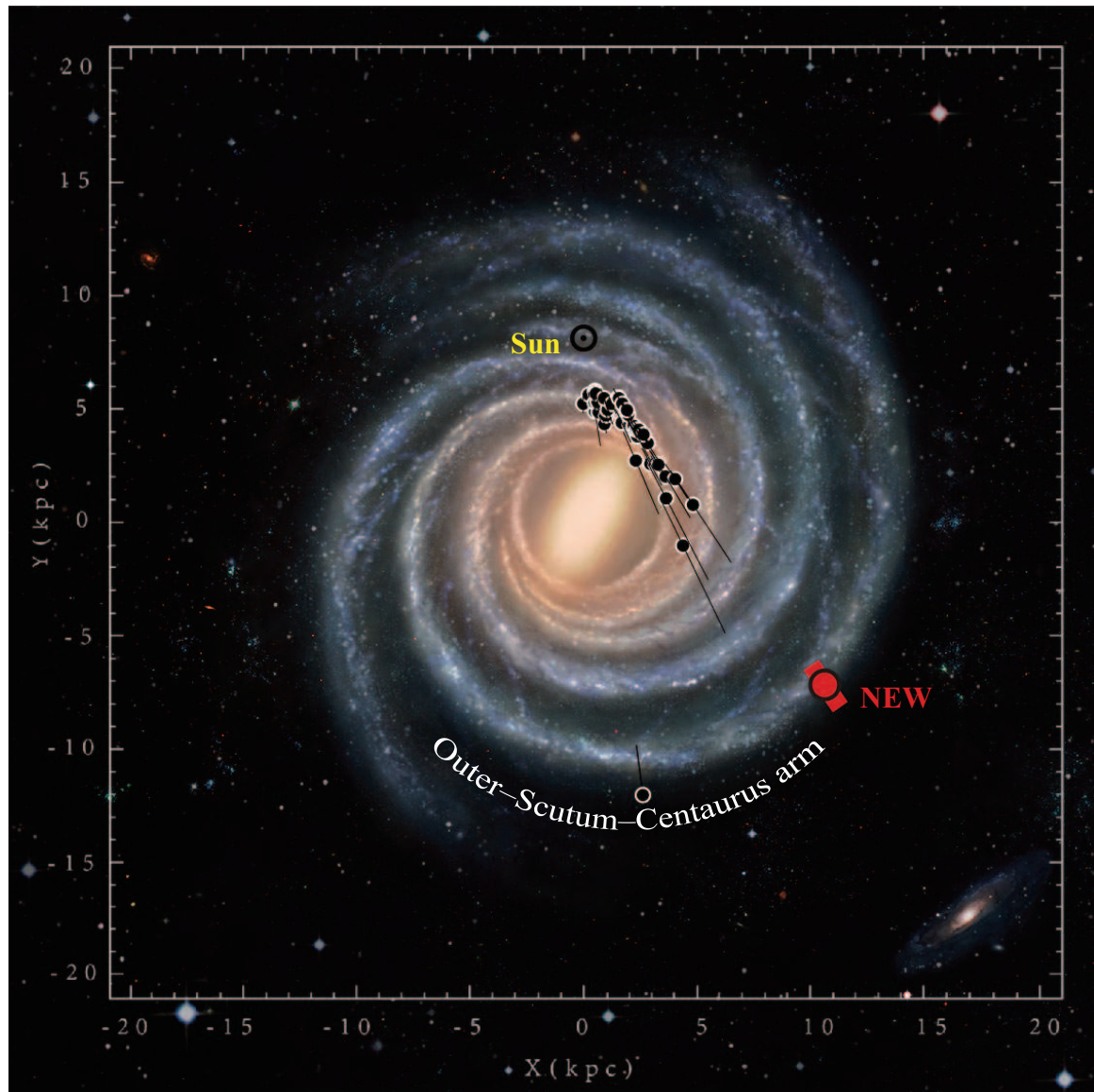


Fig. 6. The most scientifically accurate visualization of the Milky Way (at the moment) on which previous VLBI astrometric results (black circles with white borders; Reid et al. 2019; VERA Collaboration et al. 2020) for the Scutum-Centaurus arm are superimposed. The new astrometric result of G034.84–00.95 ($d = 18.6 \pm 1.0$ kpc) is emphasized by the red circle with black border. **Image Credit:** ©Xingwu Zheng & Mark Reid, BeSSeL/NJU/CfA. The background image can be downloaded from the URL⁸.

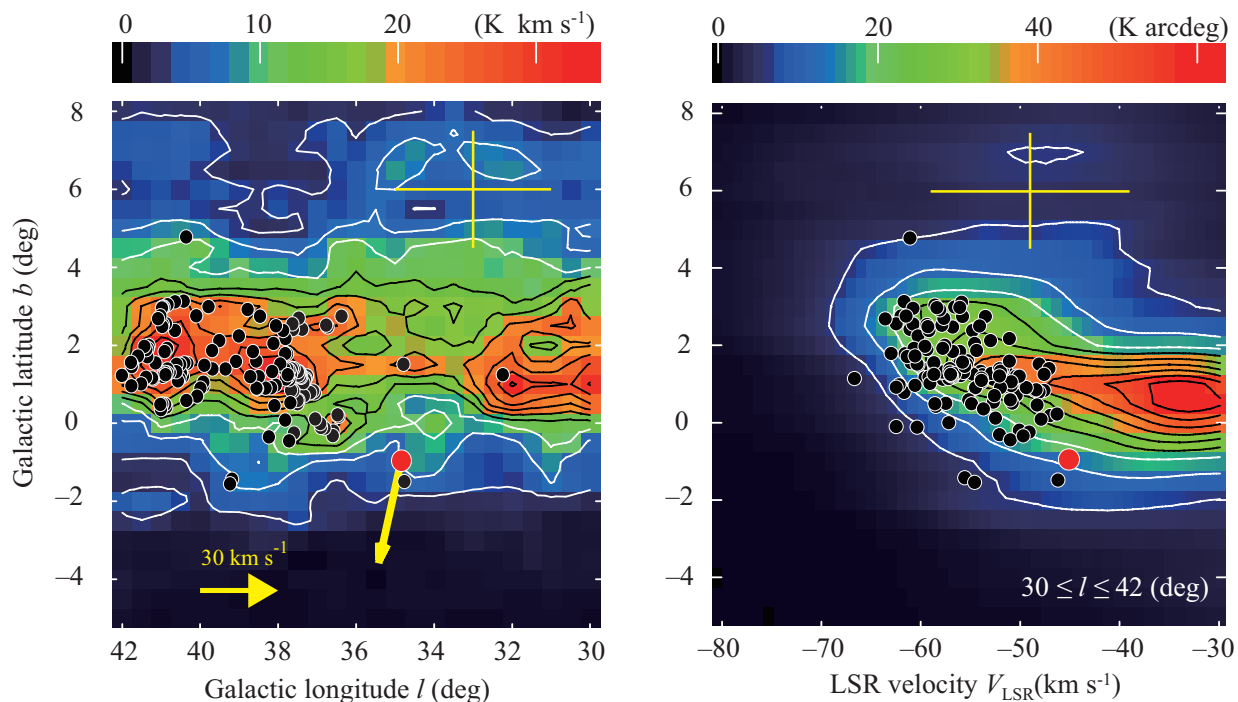


Fig. 7. (Left) Velocity-integrated H I emission in Galactic coordinates, obtained by integrating LAB H I survey data (Kalberla et al. 2005). The integration range of LSR velocity is consistent with the Outer-Scutum-Centaurus arm (see Fig. 2 of Sun et al. 2017 for the range). The H I contour starts at 3.4 (K km s^{-1}) and increases by a factor of n where $n = 2, 3, \dots, 8, 9$. Circles show CO clouds associated with the Outer-Scutum-Centaurus arm, taken from Dame & Thaddeus (2011) and Sun et al. (2017). Red circle represents G034.84–00.95, while the yellow arrow displays the noncircular motion of the source. A yellow cross shows the scale of the H I supershell GS033+06–49 located at a heliocentric distance of ~ 22 kpc (Heiles 1979). (Right) Same as the Left, but for LSR velocity vs. Galactic latitude of the H I emission, integrated over the Galactic longitude range $30 \leq l \leq 42$ (deg). The H I contour starts at 6.3 (K arcdeg) and increases by a factor of n where $n = 2, 3, \dots, 8, 9$.

kpc; Cardillo et al. 2014) are observed toward similar directions of G034.84–00.95 (see Fig. 8). However, we emphasize that the parallax signature corresponding to 2.5 kpc (i.e., 0.4 mas), should be detected with KaVA if the source is located at $d = 2.5$ kpc. The small parallax result with relatively large uncertainty ($0.040^{+0.061}_{-0.028}$ mas) supports a larger distance. To confirm the validity of our parallax result quantitatively, we superimposed a larger parallax amplitude of 0.4 mas on our parallax result (see Fig. 11 in Appendix 1) and compared reduced chi-square values between both parallax results. The reduced chi-square value is increased from 1.1 to 2.9 if we apply the larger 0.4 mas parallax amplitude. Thus, the observational results can be better explained with the smaller parallax amplitude; i.e. the far distance.

To further evaluate the possibility that the source is a nearby object, we estimate peculiar (i.e., noncircular) motion and the spectral type of G034.84–00.95 at different distances (2.5 ± 0.1 kpc and 18.6 ± 1.0 kpc) in Table 3. We also derive the physical quantities of G034.79–01.38 and G035.19–00.74 for comparison. Note that the former distance of G034.84–00.95 is the variance weighted average of the distances of G034.79–01.38 and G035.19–00.74. The calculation of noncircular motion

values is based on the appendices of Sakai et al. (2015, 2020). For the derivation of bolometric luminosity, we use flux densities in IRAS four bands ($12 \mu\text{m}$, $25 \mu\text{m}$, $60 \mu\text{m}$, and $100 \mu\text{m}$) and the distance for each object (see the formulation by Wang et al. 2009). We independently estimated the bolometric luminosity of G034.84–00.95 with Spectral Energy Distribution fits in Appendix 4. We confirmed that both the methods can provide consistent results to each other.

If we assume a distance of 2.5 ± 0.1 kpc for G034.84–00.95, a significantly large noncircular motion is derived along the disk (i.e., $U_s = -48 \pm 4 \text{ km s}^{-1}$ and $V_s = -76 \pm 4 \text{ km s}^{-1}$). However, such noncircular motion is not seen for G034.79–01.38 and G035.19–00.74 (see Table 3). Backwinding the noncircular motion of G034.84–00.95 does not intersect the SNR W44 in Fig. 8. The bolometric luminosity of the source is less luminous (2.99 in $\log L/L_\odot$) than the other sources. Thus, the near distance (2.5 ± 0.1 kpc) is unlikely for G034.84–00.95.

Our distance estimate for G034.84–00.95 (18.6 ± 1.0 kpc) is also supported by the fact that a Galactic H II region associated with the OSC arm shows negative Galactic latitude at $(l, b, V_{\text{LSR}}) = (39^\circ 183, -1^\circ 422, -54.9 \text{ km s}^{-1})$ (Anderson et al. 2015). If our distance estimate is correct, G034.84–00.95 is regarded as a high-mass star-forming region with a bolomet-

⁸ <https://astronomy.nju.edu.cn/xtzl/EN/index.html>

Table 3. Noncircular motion and spectral type of G034.84–00.95 at different distances.

Source	U_s (km s ⁻¹)	V_s (km s ⁻¹)	W_s (km s ⁻¹)	d (kpc)	R (kpc)	z (pc)	$\log L/L_\odot$	Spectral type
Case A: Distance = 2.5 ± 0.1 kpc*								
G034.84–00.95	-48 ± 4	-76 ± 4	1 ± 2	2.5 ± 0.1	6.3 ± 0.1	-42 ± 2	2.99	Later than B3
G034.79–01.38	-7 ± 7	4 ± 7	-6 ± 8	2.6 ± 0.1	6.2 ± 0.1	-64 ± 3	3.71	Earlier than B2
G035.19–00.74	-4 ± 7	-8 ± 7	-8 ± 5	2.2 ± 0.2	$6.5_{-0.2}^{+0.1}$	-29 ± 3	4.28	Earlier than B0.5
Case B: Distance = 18.6 ± 1.0 kpc[†]								
G034.84–00.95	-6 ± 10	-7 ± 24	-38 ± 16	18.6 ± 1.0	$12.8_{-0.9}^{+1.0}$	-309 ± 17	4.73	O8.5

Column 1: source name; Columns 2-4: noncircular motion components toward the Galactic center, in the direction of the Galactic rotation, and toward the north Galactic pole, respectively; Column 5: heliocentric distance; Column 6: Galactocentric distance; Column 7: Galactic height; Column 8: Bolometric luminosity estimated from infrared flux densities in four bands (see Wang et al. 2009); Column 9: Spectral type of Zero Age Main Sequence (see Panagia 1973).

* Variance weighted average of the distances of G034.79–01.38 and G035.19–00.74.

[†] Our result (see the text for details).

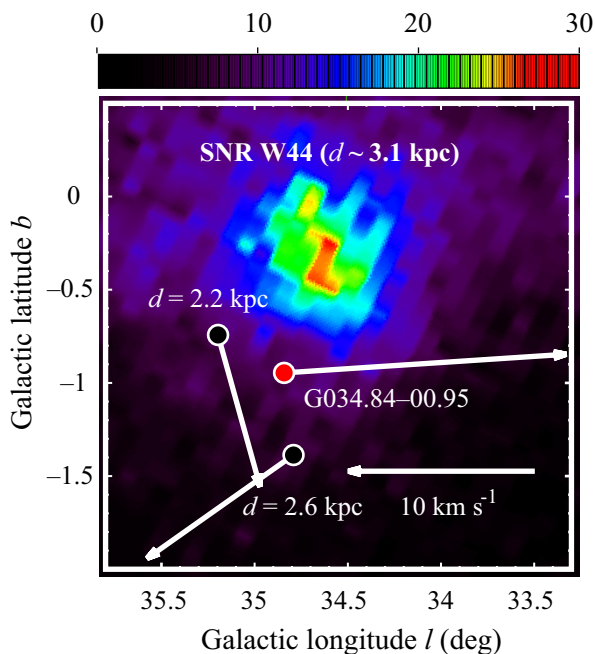


Fig. 8. Fermi-LAT (1–3 GeV) intensity map (Atwood et al. 2009)⁹ of the supernova remnant W44 on which VLBI astrometric results are superimposed. The intensity is shown by colors in units of (photon cm⁻¹ s⁻¹ sr⁻¹). The vectors show noncircular motion of the maser sources derived from the VLBI astrometric results, referring to the Case A of Table 3 where the heliocentric distance to G034.84–00.95 (red circle) is assumed to be 2.5 ± 0.1 kpc.

ric luminosity of 4.73 (in $\log L/L_\odot$) and a spectral type of O8.5. Also, the source is located at a Galactic height z of -309 ± 17 pc (see Table 3). The source is consistent with the Galactic height range ($-500 \text{ pc} < z < 1500 \text{ pc}$) of Extreme Outer Galaxy CO clouds (Sun et al. 2017). The source would show large noncircular motion perpendicular to the disk ($W_s = -38 \pm 16 \text{ km s}^{-1}$) at a distance of 18.6 ± 1.0 kpc. We will discuss a possible origin of the vertical motion in the next subsection.

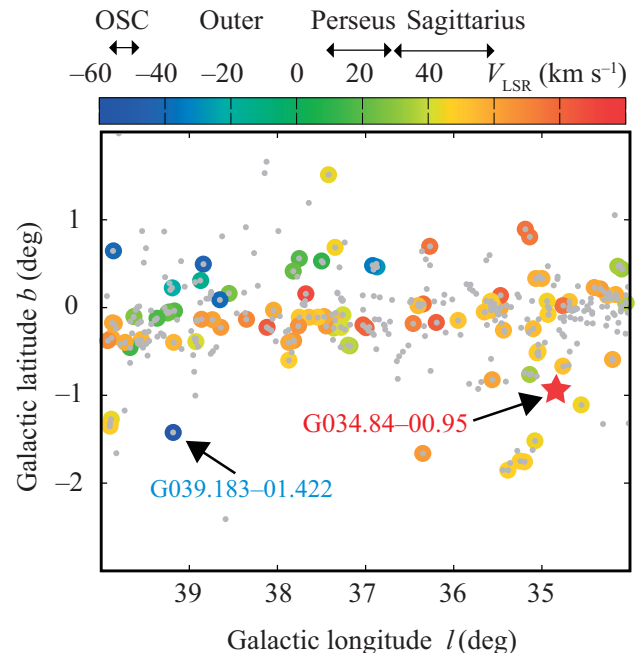


Fig. 9. Spatial distribution of Galactic H II regions in Galactic coordinates (gray circles; Anderson et al. 2014, 2015). G034.84–00.95 indicated by the red star, is superimposed on the plot. Color displays LSR velocity for a part of the H II regions. Horizontal arrows on the color bar show expected velocity ranges for individual spiral arms based on Sun et al. (2017) and Reid et al. (2019). Note that OSC is the Outer-Scutum-Centaurus arm. The expected velocity range is not shown for the Outer arm, since no VLBI astrometric results for the arm are available in the Galactic longitude range $l = [34^\circ:40^\circ]$. Black arrows emphasize G034.84–00.95 and the H II region G039.183–01.422 which are associated with the OSC arm.

⁹ Downloaded using the software *Aladin Sky Atlas* (Bonnarel et al. 2000;

5.2 Vertical motion perpendicular to the disk

Fast vertical motion ($V_z \geq 20 \text{ km s}^{-1}$) has been discussed in the context of the expansion of the NGC281 superbubble (Sato et al. 2008), whereas Sakai et al. (2022) discussed it in another context as originating in cloud collisions with the Galactic disk. The H I supershell GS033+06–49 exhibits a Galactic longitude and LSR velocity similar to G034.84–00.95 (see Fig. 7), and a kinematic distance of $\sim 22 \text{ kpc}$ was estimated for the H I supershell (Heiles 1979). If we assume the same rotation curve for G034.84–00.95 and the H I supershell, then the difference of individual distances between the two objects should become smaller. The existence of the H I supershell indicates that gas circulation occurs between the outer Galactic disk and halo at a Galactocentric distance $>12 \text{ kpc}$ in the first Galactic quadrant. Note that a physical relationship between G034.84–00.95 and the H I supershell is unclear, because G034.84–00.95 is deviated from the H I supershell by $\sim 7^\circ$ in the direction of Galactic latitude.

We check the distribution of H II regions around G034.84–00.95, since the NGC281 superbubble is surrounded by an H II region. We refer to the catalog of Anderson et al. (2014) which contains $>8,000$ H II regions and H II region candidates. The catalog was made based on Wide-Field Infrared Survey Explorer (WISE) observations which have sufficient sensitivity to detect mid-infrared emission from H II regions located anywhere in the Galactic disk. However, we cannot find H II regions around G034.84–00.95 in Figures 9 and 10. Anderson et al. (2015) listed four OSC H II regions in the Galactic longitude range $30^\circ \leq l \leq 42^\circ$. Only one H II region in G039.183–01.422 shows negative Galactic latitude among the four H II regions.

We also checked large scale distribution of H I emission in Galactic coordinates, since Sakai et al. (2022) found a H I stream toward the direction of noncircular motion of G050.28–00.39 (see Fig. 6 of Sakai et al. 2022). We could not find any H I stream below G034.84–00.95 and the Galactic plane.

We failed to find a robust origin of the fast vertical motion of G034.84–00.95 at this moment. Further astrometric observations toward the OSC arm are required in the future. For instance, G039.183–01.422 contains both an H II region and an H₂O maser, and is a valuable candidate for VLBI astrometry (see Figures 9 and 10).

6 Summary

We conducted VLBI astrometry toward the star-forming region G034.84–00.95 (Table 1) for studying the structure and kinematics of the Extreme Outer Galaxy. We overcame observational difficulty reported in previous VERA astrometry for a

Boch & Fernique 2014).

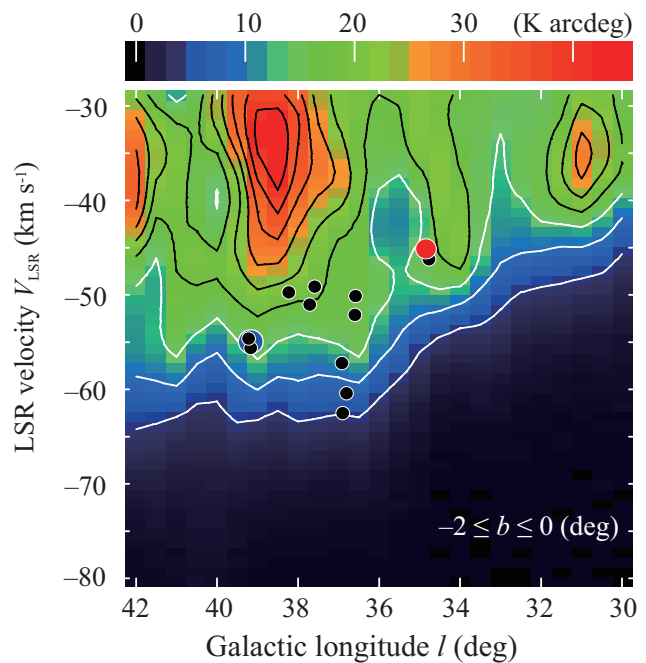


Fig. 10. Longitude-velocity diagram of H I emission, obtained by integrating LAB H I survey data from Kalberla et al. (2005) over the latitude range $-2 \leq b \leq 0$ (deg). The H I contour starts at 4.4 (K arcdeg) and increases by a factor of n where $n = 2, 3, \dots, 8, 9$. Black circles show CO clouds associated with the OSC arm, taken from Dame & Thaddeus (2011) and Sun et al. (2017). Red circle represents G034.84–00.95, while the blue one shows the H II region G039.183–01.422.

source close to the celestial equator (Kurayama et al. 2011) by using KaVA consisting of VERA and KVN (see Fig. 4). We measured the proper motion of the source to be $(\mu_\alpha \cos \delta, \mu_\delta) = (-1.61 \pm 0.18, -4.29 \pm 0.16) \text{ mas yr}^{-1}$ in equatorial coordinates (Table 2 and Fig. 5), whereas we could not obtain the reliable parallax ($0.040^{+0.061}_{-0.028} \text{ mas}$).

We estimated the source’s kinematic distances through LSR velocity V_{LSR} and proper motion in the direction of Galactic longitude μ_l , which are $d_{V_{\text{LSR}}} = 17.7^{+2.0}_{-1.6} \text{ kpc}$ and $d_{\mu_l} = 18.9 \pm 1.1 \text{ kpc}$, respectively (Table 2 and Fig. 5). We determined the 2D kinematic distance of the source to be $18.6 \pm 1.1 \text{ kpc}$ by the variance weighted average of both $d_{V_{\text{LSR}}}$ and d_{μ_l} (Fig. 6). The 2D kinematic distance places the source in the Outer-Scutum-Centaurus arm.

We evaluated the assumption that G034.84–00.95 is a nearby source ($d \sim 2.5 \text{ kpc}$) and is physically related to G034.79–01.38 ($d = 2.6 \pm 0.1 \text{ kpc}$), G035.19–00.74 ($d = 2.2 \pm 0.2$), and the supernova remnant W44 ($d \sim 3.1 \text{ kpc}$) (Table 3 and Fig. 8). This is because the source shows negative latitude although the outer Galactic disk is warped toward the north Galactic pole in the 1st Galactic quadrant. G034.84–00.95 should show large ($>80 \text{ km s}^{-1}$) noncircular motion parallel to the disk if the source is nearby. On the other hand, G034.79–01.38 ($d = 2.6 \pm 0.1 \text{ kpc}$) and G035.19–00.74 ($d =$

2.2 ± 0.2) display smaller noncircular motion $< 10 \text{ km s}^{-1}$. Backwinding the noncircular motion of G034.84–00.95 does not intersect the SNR W44 in Fig. 8. Thus, we rejected the case for a nearby distance ($d \sim 2.5 \text{ kpc}$) for G034.84–00.95. Our conclusion is supported by the fact that Anderson et al. (2015) found a H II region associated with the OSC arm at a negative Galactic latitude (i.e., G039.183–01.422).

We discussed possible origins of the fast vertical motion in G034.84–00.95 ($W_s = -38 \pm 16 \text{ km s}^{-1}$ at $d_{2D} = 18.6 \pm 1.1 \text{ kpc}$), which are the expansion of the superbubble (i.e., supernova explosions) and cloud collision with the Galactic disk. Gas circulation may occur between the outer Galactic disk around G034.84–00.95 with a Galactocentric distance of 12.8 kpc and halo by considering the fact that the H I supershell GS033+06–49 is located at a kinematic distance similar to that of G034.84–00.95. However, we could not find a physical origin of the vertical motion for the following reasons. We could not find an H II region around G034.84–00.95 (Figures 9 and 10). Also, we could not confirm H I streams toward the direction of the noncircular motion of G034.84–00.95. Thus, further VLBI astrometry toward the OSC arm is important in the future. Another target, G039.183–01.422, associated with the OSC arm, is a valuable candidate for this purpose since the source contains H II region and H₂O (22 GHz) masers.

Acknowledgments

We deeply thank the anonymous referee for thoughtful and constructive comments which greatly improved the quality and robustness of the paper. We acknowledge Dr. Yoshiaki Tamura for analyzing JMA data for tropospheric calibration of KVN. We deeply thank Dr. Mark J. Reid, Dr. Tomoya Hirota and Dr. Koichiro Sugiyama for stimulating discussions and valuable comments. We acknowledge EAVN (East Asian VLBI Network) project members for their support on observations, correlations, and data reductions. Data analysis was in part carried out on a common use data analysis computer system at the Astronomy Data Center, ADC, of NAOJ. This research made use of sedcreator (Fedriani et al. 2022).

BZ was supported by the National Natural Science Foundation of China (Grant No. U2031212 and U1831136), and Shanghai Astronomical Observatory, Chinese Academy of Sciences (Grant No. N2020-06-19-005).

References

- Anderson, L. D., Armentrout, W. P., Johnstone, B. M., et al. 2015, *ApJS*, 221, 16
- Anderson, L. D., Bania, T. M., Balser, D. S., et al. 2014, *ApJS*, 212, 1
- Atwood, W. B., Abdo, A. A., Ackermann, M., et al. 2009, *ApJ*, 697, 1071
- Bailer-Jones, C. A. L. 2015, *PASP*, 127, 994
- Benjamin, R. A., Churchwell, E., Babler, B. L., et al. 2003, *PASP*, 115, 953
- Boch, T., & Fernique, P. 2014, in *Astronomical Society of the Pacific Conference Series*, Vol. 485, *Astronomical Data Analysis Software and Systems XXIII*, ed. N. Manset & P. Forshay, 277
- Bonnarel, F., Fernique, P., Bienaymé, O., et al. 2000, *A&AS*, 143, 33
- Cardillo, M., Tavani, M., Giuliani, A., et al. 2014, *A&A*, 565, A74
- Caswell, J. L., & Breen, S. L. 2010, *MNRAS*, 407, 2599
- Cutri, R. M., Wright, E. L., Conrow, T., et al. 2012, Explanatory Supplement to the WISE All-Sky Data Release Products, Explanatory Supplement to the WISE All-Sky Data Release Products
- Dame, T. M., & Thaddeus, P. 2011, *ApJL*, 734, L24
- Digel, S., de Geus, E., & Thaddeus, P. 1994, *ApJ*, 422, 92
- Fedriani, R., Tan, J. C., Telkamp, Z., et al. 2022, arXiv e-prints, arXiv:2205.11422
- Foreman-Mackey, D., Hogg, D. W., Lang, D., & Goodman, J. 2013, *PASP*, 125, 306
- Gaia Collaboration. 2022, *VizieR Online Data Catalog*, I/355
- Gutermuth, R. A., & Heyer, M. 2015, *AJ*, 149, 64
- Heiles, C. 1979, *ApJ*, 229, 533
- Herschel Point Source Catalogue Working Group, Marton, G., Calzoletti, L., et al. 2020, *VizieR Online Data Catalog*, VIII/106
- Jike, T., Manabe, S., & Tamura, Y. 2018, *Journal of the Geodetic Society of Japan*, 63, 193
- Kalberla, P. M. W., Burton, W. B., Hartmann, D., et al. 2005, *A&A*, 440, 775
- Kamezaki, T., Nakagawa, A., Omodaka, T., et al. 2012, *PASJ*, 64, 7
- Kawaguchi, N., Sasao, T., & Manabe, S. 2000, in *Society of Photo-Optical Instrumentation Engineers (SPIE) Conference Series*, Vol. 4015, *Proc. SPIE*, ed. H. R. Butcher, 544–551
- Kim, S.-H., Martin, P. G., & Hendry, P. D. 1994, *ApJ*, 422, 164
- Kurayama, T., Nakagawa, A., Sawada-Satoh, S., et al. 2011, *PASJ*, 63, 513
- Lee, S.-S., Oh, C. S., Roh, D.-G., et al. 2015, *Journal of Korean Astronomical Society*, 48, 125
- McCarthy, D. D. 1996, *IERS Technical Note*, 21, 1
- Nagayama, T., Kobayashi, H., Omodaka, T., et al. 2015, *PASJ*, 67, 65
- Nagayama, T., Kobayashi, H., Hirota, T., et al. 2020, *PASJ*, 72, 52
- Newville, M., Stensitzki, T., Allen, D. B., et al. 2016, *Lmfit: Non-Linear Least-Square Minimization and Curve-Fitting for Python*, *Astrophysics Source Code Library*, record ascl:1606.014, ascl:1606.014
- Ouyang, X.-J., Chen, X., Shen, Z.-Q., et al. 2022, *ApJS*, 260, 51
- Panagia, N. 1973, *AJ*, 78, 929
- Reid, M. J. 2022, arXiv e-prints, arXiv:2205.06903
- Reid, M. J., Dame, T. M., Menten, K. M., & Brunthaler, A. 2016, *ApJ*, 823, 77
- Reid, M. J., Menten, K. M., Brunthaler, A., et al. 2019, *ApJ*, 885, 131
- Robitaille, T. P., Meade, M. R., Babler, B. L., et al. 2008, *AJ*, 136, 2413
- Sakai, N., Nakanishi, H., Kurahara, K., et al. 2022, *PASJ*, 74, 209
- Sakai, N., Reid, M. J., Menten, K. M., Brunthaler, A., & Dame, T. M. 2019, *ApJ*, 876, 30
- Sakai, N., Nakanishi, H., Matsuo, M., et al. 2015, *PASJ*, 67, 69
- Sakai, N., Nagayama, T., Nakanishi, H., et al. 2020, *PASJ*, 72, 53
- Sanna, A., Reid, M. J., Dame, T. M., Menten, K. M., & Brunthaler, A. 2017, *Science*, 358, 227
- Sato, M., Hirota, T., Honma, M., et al. 2008, *PASJ*, 60, 975
- Sivia, D., & Skilling, J. 2006, *Data Analysis: A Bayesian Tutorial* (2nd ed.; New York: Oxford Univ. Press)
- Skrutskie, M. F., Cutri, R. M., Stiening, R., et al. 2006, *AJ*, 131, 1163
- Sofue, Y. 2011, *PASJ*, 63, 813
- Spitzer Science, C. 2009, *VizieR Online Data Catalog*, II/293
- Sun, Y., Su, Y., Zhang, S.-B., et al. 2017, *ApJS*, 230, 17
- Sun, Y., Xu, Y., Yang, J., et al. 2015, *ApJL*, 798, L27

Table 4. Astrometric results of G034.84–00.95 relative to J1851+0035.

DOY (day)	Position offset		V_{LSR} km s ⁻¹
	$\Delta\alpha$ (mas)	$\Delta\delta$ (mas)	
248	0.682±0.082	0.178±0.092	-44.0
284	0.689±0.068	-0.446±0.063	-44.0
308	0.448±0.040	-0.603±0.039	-44.0
355	0.197±0.020	-1.238±0.027	-44.0
394	-0.071±0.015	-1.560±0.017	-44.0
423	-0.656±0.014	-1.502±0.018	-44.0
447	-0.470±0.018	-1.936±0.020	-44.0
475	-0.612±0.047	-2.321±0.060	-44.0
631	-1.206±0.072	-4.681±0.108	-44.0
682	-1.204±0.026	-4.972±0.029	-44.0
813	-1.648±0.091	-6.501±0.092	-44.0

Column 1: day of year since 2019; Columns 2-3: position offset values of G034.84–00.95 in R.A. and Decl., respectively, relative to $(\alpha, \delta) = (18^{\text{h}}58^{\text{m}}17^{\text{s}}.6726, 01^{\circ}16'06''.400)$ in J2000. Positional errors are statistical errors; Column 4: LSR velocity (V_{LSR}) of the maser emission.

Sun, Y., Xu, Y., Chen, X., et al. 2018, ApJ, 869, 148

Thompson, A. R., Moran, J. M., & Swenson, George W., J. 2017, Interferometry and Synthesis in Radio Astronomy, 3rd Edition, doi:10.1007/978-3-319-44431-4

Urquhart, J. S., Morgan, L. K., Figura, C. C., et al. 2011, MNRAS, 418, 1689

van Moorsel, G., Kemball, A., & Greisen, E. 1996, in Astronomical Society of the Pacific Conference Series, Vol. 101, Astronomical Data Analysis Software and Systems V, ed. G. H. Jacoby & J. Barnes, 37

VERA Collaboration, Hirota, T., Nagayama, T., et al. 2020, PASJ, 72, 50

Wang, K., Wu, Y. F., Ran, L., Yu, W. T., & Miller, M. 2009, A&A, 507, 369

Yamauchi, A., Yamashita, K., Honma, M., et al. 2016, PASJ, 68, 60

Appendix 1 Supplemental materials

We show supplemental materials to further document observational results of G034.84–00.95 (Table 4; Figures 12 and 11).

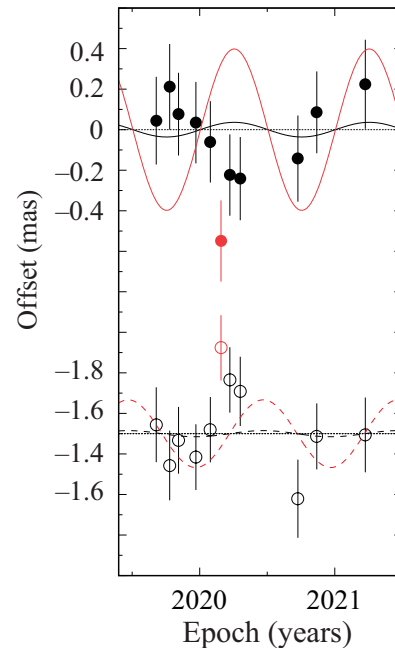


Fig. 11. Same as Fig. 5 (middle), but with a parallax amplitude of 0.4 mas superimposed (red solid and dashed curves). Black solid and dashed curves display a parallax amplitude of 0.04 mas. Based on reduced chi-square values, a model with the smaller parallax amplitude can better explain the observational results (see the text for details).

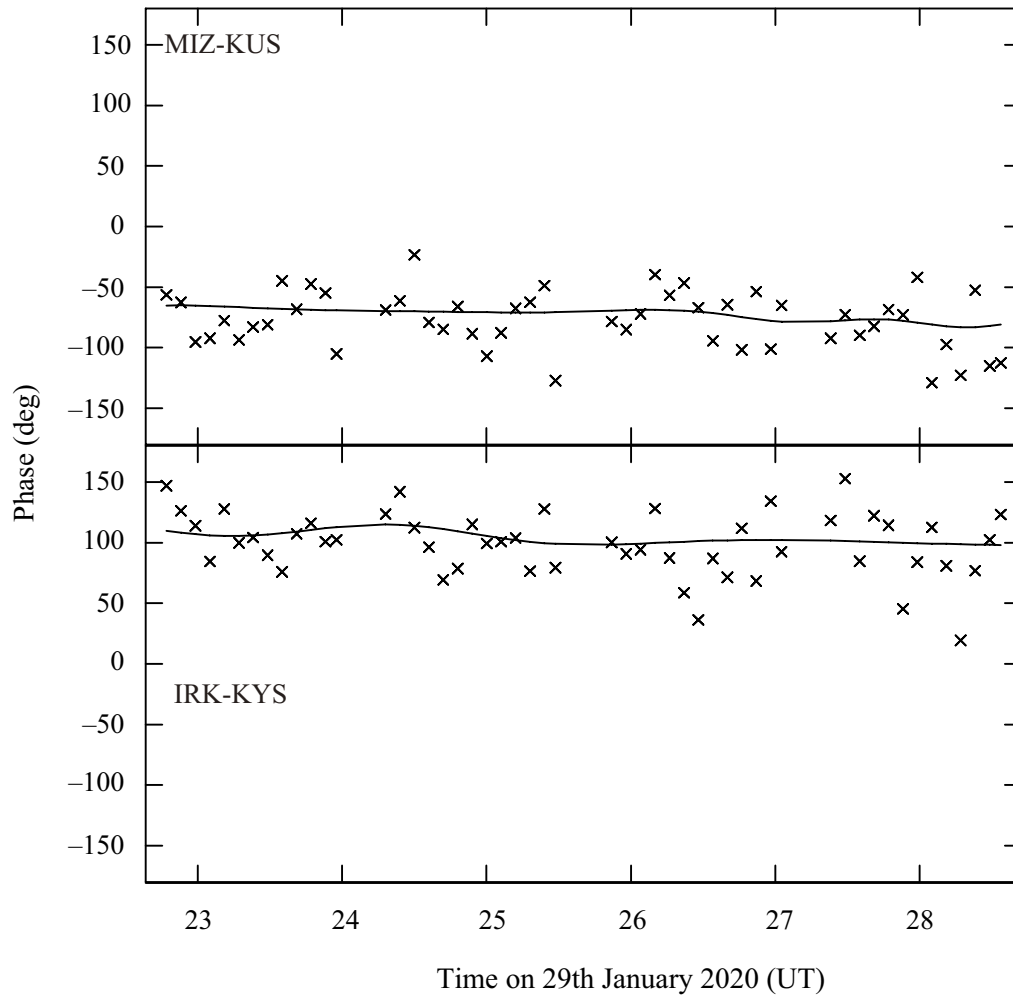


Fig. 12. Corrected phases by phase referencing are shown for G034.84–00.95 where horizontal axis is time in (UT). (**Top**) and (**Bottom**) panels display the phases for Mizusawa-Ulsan and Iriki-Yonsei baselines, respectively. The data of epoch E (see Table 1) is used. Each cross showing the phase, is created by integrating visibilities over 6 (min) while black curves show models taken from AIPS CC (Clean Component) files.

Appendix 2 A Bayesian analysis

We determined up to seven model parameters (i.e., parallax, reference positions, proper motion components, and systematic errors in R.A. and Decl., respectively) with Bayesian statistics (see a part of the model parameters in Table 5). For this purpose, we referred to a Fortran program developed by the VLBA BeSSeL project (Dr. Mark J. Reid). Note that we developed a Python program for our analysis. We used the Python package `lmfit` (Newville et al. 2016) for fitting models to R.A. and Decl. data simultaneously. Based on Bayes's theorem, the posterior probability distribution is described as

$$p(\boldsymbol{\theta}|\{y_i\}_{i=1}^N) = \frac{p(\{y_i\}_{i=1}^N|\boldsymbol{\theta})p(\boldsymbol{\theta})}{p(\{y_i\}_{i=1}^N)} \sim p(\{y_i\}_{i=1}^N|\boldsymbol{\theta})p(\boldsymbol{\theta}) \quad (\text{A1})$$

where $p(\{y_i\}_{i=1}^N|\boldsymbol{\theta})$ and $p(\boldsymbol{\theta})$ are the likelihood function and prior, respectively. Note that $p(\{y_i\}_{i=1}^N)$ is a normalization constant. The model parameters are contained in $\boldsymbol{\theta}$, and y_i show observational results.

To identify outlier data, we firstly assumed that data uncertainties obeyed a probability density function (PDF) with Lorentzian-like wings, which makes the fits insensitive to outliers (see ‘‘conservative formulation’’ of Sivia & Skilling 2006). The observational results in epoch ‘‘F’’ (see Table 1) deviated by $>3\text{-}\sigma$ from the PDF. We made two data sets with and without the outlier, and evaluated both the data sets in Table 5.

To draw posterior probability distributions for individual model parameters, we used the python package `emcee` which is an MIT licensed pure-Python implementation of Goodman & Weare's Affine Invariant Markov chain Monte Carlo (MCMC) Ensemble sampler (Foreman-Mackey et al. 2013).

Since the posterior consists of the likelihood and the prior(s), we explain our definitions of the likelihood and the prior(s) in the following subsections.

A.2.1 Likelihood function, $p(\{y_i\}_{i=1}^N|\boldsymbol{\theta})$

We used a Gaussian likelihood as

$$p(\{y_i\}_{i=1}^N|\boldsymbol{\theta}) = \frac{1}{\sqrt{2\pi(\sigma_i^2 + \sigma_{\text{sys}}^2)}} \exp\left[-\frac{(\{y_i\}_{i=1}^N - \hat{y}_i)^2}{2(\sigma_i^2 + \sigma_{\text{sys}}^2)}\right] \quad (\text{A2})$$

where \hat{y}_i and σ_{sys} are model (e.g., see equations 1-2 in Kamezaki et al. 2012) and systematic error, respectively, for R.A. or Decl. data. The total likelihood is the product of all the individual likelihoods. For computing this, we show the natural logarithm of the total likelihood as

$$\ln \prod_{i=1}^N p(\{y_i\}_{i=1}^N|\boldsymbol{\theta}) = -\frac{1}{2} \sum_{i=1}^N \left[\frac{(\{y_i\}_{i=1}^N - \hat{y}_i)^2}{\sigma_i^2 + \sigma_{\text{sys}}^2} + \ln(2\pi\{\sigma_i^2 + \sigma_{\text{sys}}^2\}) \right]. \quad (\text{A3})$$

A.2.2 Prior probability distributions, $p(\boldsymbol{\theta})$

Priors reflect our knowledge about the model parameters. We used a flat prior for reference positions in R.A. and Decl., respectively. For systematic errors in R.A. or Decl., we adopted a Jeffreys prior as

$$p(\sigma_{\text{sys}}) \propto \frac{1}{\sigma_{\text{sys}}}. \quad (\text{A4})$$

Bailer-Jones (2015) recommended not to use a flat prior for the distance converted via the reciprocal of the trigonometric parallax (i.e., $d = \frac{1}{\pi}$). This is because the posterior probability distribution of the distance based on a flat prior shows a large tail toward large distance if the fractional parallax error is greater than 20% (see Fig. 1 of Bailer-Jones 2015). Thus, we assumed the following prior:

$$p(\pi) \begin{cases} 1 & (0.01 \leq \pi) \\ \left(\frac{\pi}{0.01}\right)^2 & (0.01 * 0.1 \leq \pi < 0.01) \\ \left(\frac{0.01 * 0.1}{\pi}\right)^2 & (\pi < 0.01 * 0.1) \end{cases} \quad (\text{A5})$$

for the parallax. Note that the parallax of 0.01 mas converts to a distance of 100 kpc. The distance is well larger than the size of the Milky Way, and perhaps we could use a larger threshold than 0.01 mas. This prior naturally forces the parallax to be positive. We evaluated both a flat prior and Eq. A5 for the parallax in Table 5.

Regarding proper motion components in R.A. and Decl. (i.e., slopes in time vs. positional offset values), we adopted the following prior as

$$p(\mu) \propto (1 + \mu)^{-3/2}. \quad (\text{A6})$$

This prior allows a proper motion not to be biased to a larger value as discussed in an unpublished paper, Jaynes, E. T., (1991)⁸. Note that the proper motion (i.e., slope in a line fitting) is not biased even with a flat prior if the number of data is enough.

Table 5. Parallax and proper motion fits with different Bayesian approaches.

ID	Data	π	$\mu_{\alpha} \cos \delta$	μ_{δ}	Systematic errors		χ^2_{ν}	AIC	BIC	π prior	Memo
					R.A.	Decl.					
		(mas)	(mas yr ⁻¹)	(mas yr ⁻¹)	(mas)	(mas)					
ALL observational epochs are used.											
A1n	RA	-0.16 ± 0.08	$-1.49^{+0.15}_{-0.14}$	—	0.20	—	1.1	1.4	3.0	no	
A1y	RA	$0.03^{+0.06}_{-0.15}$	-1.54 ± 0.18	—	0.25	—	1.1	6.8	8.4	yes	
A2n	Decl	$0.28^{+0.36}_{-0.37}$	—	-4.32 ± 0.15	—	0.22	1.1	3.0	4.6	no	
A2y	Decl	$0.38^{+0.32}_{-0.24}$	—	-4.33 ± 0.15	—	0.21	1.2	2.9	4.5	yes	
A3n	RA&Decl	$-0.13^{+0.09}_{-0.08}$	-1.50 ± 0.15	-4.30 ± 0.16	0.20	0.23	1.1	4.1	11.7	no	
A3y	RA&Decl	$0.04^{+0.06}_{-0.03}$	$-1.56^{+0.18}_{-0.19}$	-4.31 ± 0.15	0.26	0.21	1.1	8.6	16.3	yes	
Observation epoch “F” (see Table 1) is removed with conservative formulation of (Sivia & Skilling 2006).											
F1n	RA	$-0.10^{+0.07}_{-0.06}$	$-1.55^{+0.12}_{-0.11}$	—	0.14	—	1.3	-3.0	-2.0	no	
F1y	RA	$0.03^{+0.05}_{-0.02}$	-1.60 ± 0.14	—	0.19	—	1.2	1.1	2.3	yes	
F2n	Decl	$0.33^{+0.27}_{-0.28}$	—	-4.31 ± 0.12	—	0.16	1.2	-2.0	-1.0	no	
F2y	Decl	$0.38^{+0.25}_{-0.21}$	—	-4.31 ± 0.11	—	0.15	1.3	-2.3	-1.1	yes	
F3n	RA&Decl	$-0.08^{+0.07}_{-0.06}$	$-1.56^{+0.12}_{-0.11}$	-4.29 ± 0.13	0.15	0.18	1.2	-4.7	2.3	no	best
F3y	RA&Decl	$0.04^{+0.06}_{-0.03}$	-1.61 ± 0.14	-4.29 ± 0.12	0.20	0.16	1.1	-1.1	5.9	yes	preferred

Column 1: fitting ID; Column 2: data type (RA = only R.A. data is used; Decl = only Decl. data is used; RA&Decl = both R.A. and Decl. data are used); Column 3: parallax; Columns 4-5; proper motion components in R.A. and Decl., respectively; Column 6-7: systematic errors in R.A. and Decl. respectively; Column 8: the reduced chi-square value; Column 9: Akaike’s Information Criterion; Column 10: Bayesian Information Criterion; Column 11: parallax prior (no = uniform prior; yes = non-uniform prior, see the text for details); Column 12: memo.

A.2.3 Results and Summary

Based on the likelihood and priors explained above, we draw posterior probability distributions of individual model parameters in the twelve Bayesian approaches (see Table 5 and Fig. 13). Proper motion results are consistent to each other in the twelve approaches while we cannot obtain a reliable parallax result in any approaches.

The fit ID “F3n” (Table 5) shows the best result based on AIC (Akaike’s Information Criterion) and BIC (Bayesian Information Criterion) values. However, the parallax result, $-0.08^{+0.07}_{-0.06}$ mas, is physically implausible in the case of fit ID F3n. Thus, we adopt the fit ID “F3y” where the parallax result is $0.04^{+0.06}_{-0.03}$ mas. Note that the proper motion error of R.A. is larger in the case of F3y compared to F3n. We varied the threshold value of the parallax prior (i.e., eq. A5) between 0.001 mas and 0.2 mas, and confirmed that our parallax result in the ID F3y was well converged (see the right-hand side of Fig. 13).

Appendix 3 Effect of maser’s internal motion on the 2D kinematic distance of G034.84–00.95

To estimate 2D kinematic distance of G034.84–00.95, we considered not only the systematic error of the motion of central star (i.e., 10 km s⁻¹), but also the noncircular motion of a Galactic spiral arm (i.e., 13 km s⁻¹) in the section 4. However, this estimation may

⁸ The unpublished paper (“Straight Line Fitting - A Bayesian Solution”) can be downloaded from the following URL maintained by Dept. Of Chemistry and Radiology, Washington University: <https://bayes.wustl.edu/etj/node2.html>

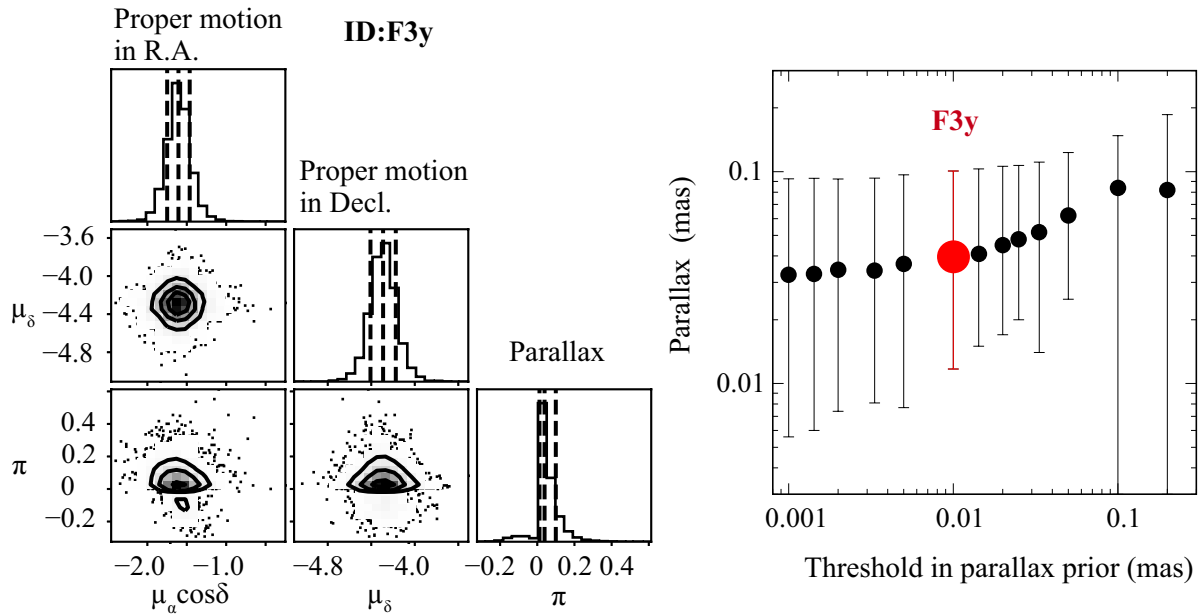


Fig. 13. (Left) Posterior probability distributions for proper motion components in R.A. and Decl., and parallax in the case of fit ID “F3Y” (see Table 5). Vertical dashed lines show the 16th, 50th, and 84th percentiles of the samples for individual model parameters. (Right) Parallax results are shown as a function of the threshold value in the parallax prior (i.e., eq. A5). Red circle displays the result in the case of fit ID F3Y where the parallax threshold is 0.01 mas.

Table 6. 2D kinematic distances for G034.84–00.95.

V_{LSR}	μ_l	Kinematic distance			Memo
		$d_{V_{\text{LSR}}}$	d_{μ_l}	d_{2D}	
(km s^{-1})	(mas yr^{-1})	(kpc)	(kpc)	(kpc)	
-45.1 ± 13.2	-4.55 ± 0.25	$17.7^{+2.0}_{-1.6}$	18.9 ± 1.1	$18.6 \pm 0.8^*$	Our best estimate [†] .
-5.1 ± 13.2	-4.55 ± 0.25	13.8 ± 1.0	18.9 ± 1.1	$16.1 \pm 3.6^*$	V_{LSR} is shifted by 40 km s^{-1} .
-45.1 ± 13.2	-4.10 ± 0.25	$17.7^{+2.0}_{-1.6}$	21.1 ± 1.3	$20.1 \pm 2.4^*$	μ_l is shifted by 40 km s^{-1} ($= 0.45 \text{ mas yr}^{-1}$ at $d = 18.9 \text{ kpc}$).

Column 1: LSR velocity; Column 2; proper motion in the direction of Galactic longitude; Columns 3-4: kinematic distances through a LSR velocity and proper motion in the direction of Galactic longitude, respectively (see the text for details); Column 5: the weighted average of both Columns 3 and 4; Column 6: Memo.

* To examine scatters between both kinematic distances (i.e., $d_{V_{\text{LSR}}}$ and d_{μ_l}), each error represents the standard deviation.

† An average noncircular motion of a Galactic spiral arm (i.e., 13 km s^{-1} ; Sakai et al. 2019) is added in quadrature to statistical errors of V_{LSR} and μ_l (see the text for details).

Table 7. Photometric results of G034.84–00.95.

λ (μm)	F_ν (mJy)	FWHM (arcsec)	Instrument (Project)	r (arcsec)	Ref.
1.2	< 0.34	2	2MASS	0.3	Skrutskie et al. (2006)
1.6	< 1.18	2	2MASS	0.3	Skrutskie et al. (2006)
2.2	1.86±0.17	2	2MASS	0.3	Skrutskie et al. (2006)
3.6	13.75±0.08	3	Spitzer (GLIMPSE)	0.4	Spitzer Science (2009)
4.5	33.9±1.4	3	Spitzer (GLIMPSE)	0.4	Spitzer Science (2009)
5.8	64.9±1.9	3	Spitzer (GLIMPSE)	0.4	Spitzer Science (2009)
8.0	112.0±2.9	3	Spitzer (GLIMPSE)	0.4	Spitzer Science (2009)
12.0	283.6±4.2	6.5	WISE	0.3	Cutri et al. (2012)
22.0	1831±27	12	WISE	0.3	Cutri et al. (2012)
24.0	1779±32	6	Spitzer (MIPSGAL)	0.3	Gutermuth & Heyer (2015)
70.0	8957±58	5	Herschel PACS	1.5	Herschel Point Source Catalogue Working Group et al. (2020)
160.0	5390±755	13	Herschel PACS	1.1	Herschel Point Source Catalogue Working Group et al. (2020)

Column 1: observing wavelength; Column 2: flux density; Column 3: Full Width at Half Maximum of beam size (i.e., angular resolution); Column 4: instrument. Parenthesis indicates the name of a project; Column 5: angular separation from the position of 22 GHz water maser associated with G034.84–00.95; Column 6: references.

be optimistic because 22-GHz H₂O masers are typically generated in outflows of tens of km s^{−1}. Such high-velocity maser features are defined as $|V - V_{\text{LSR}}| \geq 30 \text{ km s}^{-1}$ (e.g., Caswell & Breen 2010; Urquhart et al. 2011).

To more conservatively examine the effect of the maser’s internal motion on the estimate of 2D distance (d_{2D}), we shifted LSR velocity V_{LSR} and the proper motion in the direction of Galactic longitude μ_l individually by 40 km s^{−1} in Table 6. It shows that standard deviations of 2D kinematic distances are increased (16.1±3.6 kpc or 20.1±2.4 kpc) relative to our estimate (i.e., 18.6±0.8 kpc) if only V_{LSR} or μ_l is shifted by 40 km s^{−1}. All the 2D kinematic distances are consistent with each other within errors.

The small standard deviation of our distance estimate suggests that our estimate is less affected by the maser’s internal motion. Of course, we cannot rule out the possibility that the effect of the maser’s internal motion appears in the same manner in both directions of the line of sight and Galactic longitude. To confirm the robustness of our distance estimate for G034.84–00.95, the trigonometric parallax measurement of the source will be desired as was previously done for G007.47+00.06 where d_{2D} is 20±2 kpc (Yamauchi et al. 2016) and the parallax distance d_π is 20.4^{+2.8}_{−2.2} kpc (Sanna et al. 2017).

Appendix 4 SED fits of G034.84–00.95 at different distances

To evaluate the reliability of bolometric luminosity estimates in Table 3, we independently determine bolometric luminosity with a Spectral Energy Distribution fit. We used the Python package `sedcreator` (Fedriani et al. 2022) and an extinction law by (Kim et al. 1994) for the SED fits. Photometric results of G034.84–00.95 are summarized in Table 7, while the results of SED fits are shown in Fig. 14 and Table 8.

The results of SED fits guarantee that our original estimates for the bolometric luminosity of G034.84–00.95 (i.e., Table 3) are unchanged. A bolometric luminosity $L_{\text{bol}} > 10^4 L_\odot$ is obtained at a distance of 18.6 kpc, while $L_{\text{bol}} \sim 10^3 L_\odot$ is estimated at a distance of 2.5 kpc. Other physical parameters obtained by the SED fits are listed in Table 8.

Table 8. Results of SED fits for G034.84–00.95.

ID	χ	d (kpc)	$\log L/L_{\odot}$	A_V (mag)	M_{core} (M_{\odot})	R_{core} (pc)	m_* (M_{\odot})	Σ_{cl} g cm^{-2}	t_{now} ($\times 10^5$ years)
09_01_08	76	18.6	4.87	13.9	120	0.3	24	0.1	5.0
08_01_07	118	18.6	4.48	0.8	100	0.2	16	0.1	4.1
11_01_10	122	18.6	5.52	36.5	200	0.3	48	0.1	6.8
06_02_06	204	18.6	4.42	4.1	60	0.1	12	0.316	1.7
08_01_06	231	18.6	4.23	17.8	100	0.2	12	0.1	3.5
01_03_04	200	2.5	3.06	1.0	10	0.02	4	1.0	0.7
02_01_03	375	2.5	2.28	11.8	20	0.1	2	0.1	2.1
02_01_04	398	2.5	2.84	15.1	20	0.1	4	0.1	3.1
03_01_03	477	2.5	2.38	0.0	30	0.1	2	0.1	1.9
04_01_03	545	2.5	2.43	57.0	40	0.1	2	0.1	1.7

Column 1: model ID (see Fedriani et al. 2022 for detail); Column 2: the chi-square value for a model; Column 3: heliocentric distance; Column 4: bolometric luminosity where L_{\odot} is the solar luminosity; Column 5: foreground extinction; Column 6: initial mass of the core where M_{\odot} is the solar mass; Column 7: core radius; Column 8: protostellar mass; Column 9: surface mass density of the clump environment; Column 10: the current stellar age.

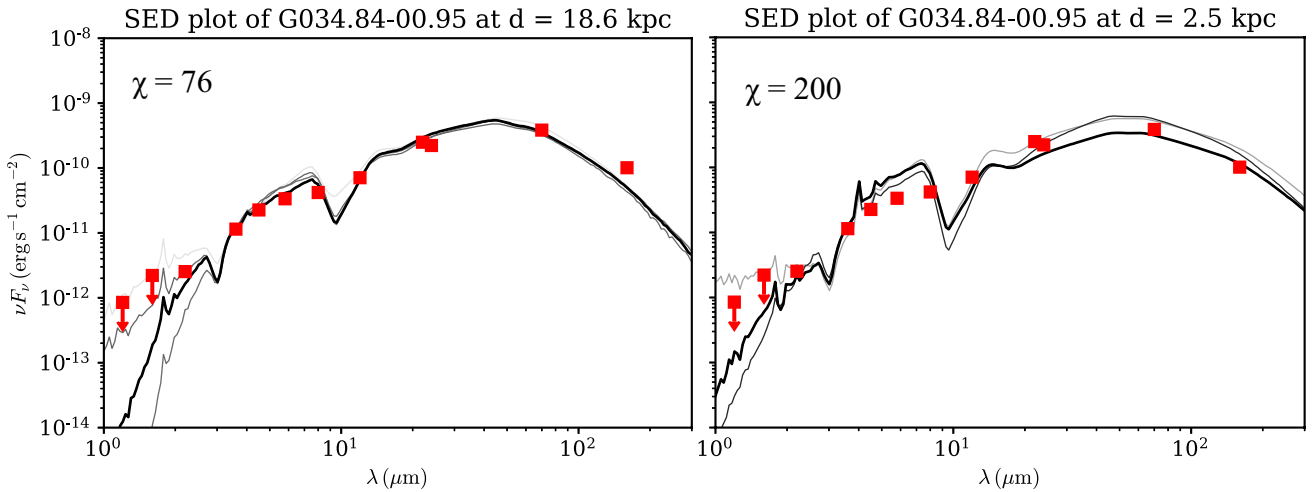


Fig. 14. Results of SED fits are shown for G034.84–00.95 at different distances 18.6 kpc (Left) and 2.5 kpc (Right). Observational results (red squares) and models (curves) are taken from Tables 7 and 8, respectively. The resultant chi-square value is shown on the upper left corner of each plot. For the SED fits, we used the Python package *sedcreator* (Fedriani et al. 2022).